Pergamon

Acta mater. 49 (2001) 4135–4147

Acta MATERIALIA

www.elsevier.com/locate/actamat

MODELING OF SHEAR INSTABILITIES OBSERVED IN CYLINDER COLLAPSE EXPERIMENTS PERFORMED ON CERAMIC POWDERS

H. D. ESPINOSA† and B. A. GAILLY

Northwestern University, 2145 Sheridan Rd., Evanston, IL 60208-3111, USA

(Received 31 August 2000; received in revised form 23 March 2001; accepted 23 March 2001)

Abstract—Brittle materials fail by microcracking and fragmentation when subjected to multiaxial loading. In some cases full comminution occurs and the material behavior becomes governed by the flow of particles. In this work a granular model developed by Anand and co-workers, based on a two-mechanism elastoplastic formulation, is extended to include rate effects and incompressibility at zero void ratio. The model parameters for Alumina and Silicon Carbide ceramic powders are identified using stress histories obtained by means of pressure-shear plate impact experiments. The model is then used to simulate the shear banding mechanism experimentally observed in thick-wall cylinder collapse experiments performed on ceramic powders (Nesterenko and co-workers). The proposed model captures the main physics of the problem and provides valuable insight in the deformation process. Initiation site and speed of propagating instabilities are obtained from the simulations. *© 2001 Acta Materialia Inc. Published by Elsevier Science Ltd. All rights reserved.*

Résumé—Les matériaux fragiles soumis à un chargement multi-axial sont susceptibles de présenter de la microfissuration et de la fragmentation. Dans certains cas, la pulvérisation peut être totale et le comportement est déterminé par l'écoulement des particules. Un modèle de comportement des matériaux granulaires, basé sur une formulation élastoplastique à deux mécanismes, a été étendu pour tenir compte de la dépendance temporelle et de l'incompressibilité sous faible fraction volumique de vide. Les paramètres décrivant les poudres d'Alumine et de Carbure de Silicium ont été déterminés en utilisant les résultats d'essais de compression-cisaillement par impact de plaques inclinées. Le modèle est ensuite utilisé pour simuler le faisceau de bandes de cisaillement observé sur des poudres de céramique dans l'expérience de collapse de cylindre épais. Le modèle proposé reproduit les principaux mécanismes du problème et donne des renseignements pertinant sur le processus de déformation. Les sites d'initiation et la vitesse de propagation des instabilités sont obtenus à partir des simulations. *© 2001 Acta Materialia Inc. Published by Elsevier Science Ltd. All rights reserved.*

Keywords: Granular; Powder consolidation; Ceramics; Internal friction; Constitutive equations

1. INTRODUCTION

In many applications, such as armor design or engine components, ceramics are used whenever high compressive strength, high hardness, high thermal resistance and low-density materials are necessary. Unfortunately, these properties are often associated with brittleness and ceramics can undergo fragmentation when subjected to multiaxial loading. It is now well known that, during an impact event, a comminuted zone also called *Mescall zone*, Mescall and Weiss [1], appears under the projectile nose. The penetration of the projectile, independently from its own mechanical properties, is driven by the behavior of the granular material and the intact surrounding ceramic. Thus understanding the shear resistance of ceramic powders under high-pressure is a fundamental step towards gaining insight of penetration processes.

Shockey *et al.* [2] studied failure of confined ceramic targets penetrated by long tungsten rods. They argued that unless the fractured material moves out of penetrator path, penetration couldn't occur. Penetration can progress only if the comminuted material flows laterally under high pressure. They recovered samples and analyzed the different kinds of cracks generated at various stages, concluding that friction, wear, and flow govern the resistance offered by confined ceramics to penetration. These remarks have been confirmed by Hauver *et al.* [3, 4] and Rapacki *et al.* [5] who showed that, if properly confined, the fragmented ceramic can offer high resistance to penetration. Null penetration has been achieved for velo-

† To whom all correspondence should be addressed. Tel.: +1-847-467-5989; Fax: +1-847-491-3540.

E-mail address: espinosa@nwu.edu (H. D. Espinosa)

PII: S1359-6454(01)00120-3

city up to 1700 m/s. These observations gave rise to the belief that ceramic internal friction and its evolution under high-strain rate and high pressure is one of the most important ballistic material properties. This belief motivated pressure-shear studies on ceramics and ceramic powders.

Two experimental techniques have been successfully used in the study of dynamic multi-axial loading of ceramics and powders. Klopp and Shockey [6], Espinosa and Clifton [7], and Sairam and Clifton [8–10] have used the oblique plate impact technique. They measured the internal friction coefficient of ceramics and confirmed that this kind of material has a Mohr-Coulomb type behavior, i.e., the yield shear stress is a linear function of the applied pressure. Moreover it seems that the friction coefficient is strain rate sensitive, or at least, that different modes of flow exist between quasi-static and dynamic deformation. Nesterenko *et al.* [11] and Shih *et al.* [12, 13] used a cylinder collapse experiment to dynamically load intact and powder ceramics. By recovering ceramic powder cylinders subjected to explosive compression waves, they found different shearing mechanisms from comminution to particle rearrangement. They also determined that the first mechanism is dominant in coarse granular SiC and fragmented ceramics while the second mostly occurs in very fine ceramic powders. These experiments have brought a better understanding of the shear behavior of granular ceramic. However, some important physical and mechanical properties cannot be measured directly. Simulating these experiments can compensate for lack of real time data, as long as a reliable and physically based models are used.

A complete model for ceramic microcracking and fragmentation including finite motion of fragments with a multiple-plane microcracking/granular formulation has been proposed elsewhere, Gailly and Espinosa [14]. In this paper we shall only focus on the granular model, which is an extension of the model previously proposed by Anand and Gu [15]. The elasto-plastic response of the powder media is modeled by a two-mechanism yield surface with sharp edges and non-associated flow rules. It includes dilatancy, cohesion and compaction of the powder.

The paper starts with a description of the model implemented in the lagragian explicit code LS-DYNA. Then, our version of the model simulates the pressure-shear impact experiments performed by Sairam and Clifton [8]. A set of material parameters is adjusted to best fit the pressure-shear experiments. This set of parameters is then used to simulate the cylinder collapse experiments performed by Nesterenko *et al.* [11].

2. COMPUTATIONAL MODEL

Here we describe a *two-mechanism* constitutive model previously developed by Anand and co-workers [15] to describe the isothermal deformation of powder media. The model is extended to the viscous regime using the Duvaut Lions scheme, see Simo *et al.* [17].

Using a corrotational Cauchy Stress measure, the constitutive behavior of the powder is given by

$$T^{\nabla} = C(T,\eta)[D-D^{p}] \tag{1}$$

where C is the fourth order elasticity tensor dependent on the relative density defined as $\eta = \rho/\rho_s$. Here ρ is the mass density of the granular material and ρ_s is the mass density of solid particles. D and D^p are respectively the total deformation rate tensor and the plastic deformation rate tensor. The latter is the sum of the contributions of the two flow mechanisms. In this model it is assumed that the plastic spin, W^P, is zero. For a justification on this assumption, see Anand and Gu [15]. The symmetric Cauchy stress tensor can be written in terms of its spectral components, namely,

$$T = \begin{cases} \sigma_1\hat{e}_1\otimes\hat{e}_1 + \sigma_2\hat{e}_2\otimes\hat{e}_2 + \sigma_3\hat{e}_3\otimes\hat{e}_3 & \text{if } \sigma_1>\sigma_2>\sigma_3, \\ \sigma_1\hat{e}_1\otimes\hat{e}_1 + \sigma_3(1-\hat{e}_1\otimes\hat{e}_1) & \text{if } \sigma_1>\sigma_2 = \sigma_3, \\ \sigma_3\hat{e}_3\otimes\hat{e}_3 + \sigma_1(1-\hat{e}_3\otimes\hat{e}_3) & \text{if } \sigma_1 = \sigma_2>\sigma_3, \end{cases} \tag{2}$$

where $\{\sigma_i|i = 1,2,3\}$ are the principal stresses and $\{\hat{e}_i|i = 1,2,3\}$ are the principal directions of stress. The usual solid mechanics convention of sign is employed, i.e., positive values correspond to tensile stresses.

The elastic properties of the granular material, i.e., Young modulus, E, and Poisson's ratio, ν, are predetermined by means of the self-consistent method proposed by Budianski [18], and then fitted to the functions,

$$E(T,\eta) = E_1 e^{E_2\eta} \tag{3}$$

$$\nu(T,\eta) = \nu_1 e^{-\nu_2\eta}$$

These quantities fully define $C(T,\eta)$ given in equation (1).

The first inelastic mechanism called *distorsion* employs a pressure-sensitive, Mohr-Coulomb type yield condition with a non-associated flow rule, i.e.,

$$\phi^{(1)} = \{\tau - s(\sigma)\} \leq 0 \tag{4}$$

$$\text{with } s(\sigma) = c + s^*\left\{\tanh\left(\frac{\mu\sigma}{s^*}\right)\right\}$$

where τ and σ represent respectively the resolved shear stress and the normal stress on a preferred slip plane, $s(\sigma)$ is a function that describes the sensitivity of the yield surface to the cohesion of the material, c, and s^* is the shear strength of the powder at high pressure. This shear strength is considered a material property.

A pair of orthonormal vectors ($m^{(\alpha)}$, $n^{(\alpha)}$) define slip system (α) as explained in Anand and Gu [15]. Here the unit vector $m^{(\alpha)}$ denotes the slip direction and $n^{(\alpha)}$ is a unit vector normal to the slip plane. In the case of powders materials there are no preferred slip directions within the microstructure. Hence, the principal directions of stress determine the directions in which the material flows and dilates or contracts as a result. For a discussion of this feature see Spencer [19, 20], Mehrabadi and Cowin [21] and Nemat-Nasser *et al.* [22].

The potential slip systems are chosen such that the yield function $\phi^{(f)}$ is a maximum. This results in

$$\tau = \frac{1}{2}\sin(2\xi)(\sigma_1-\sigma_3)\geq 0 \tag{5}$$

$$\sigma = -\frac{1}{2}(\sigma_1 + \sigma_3) + \frac{1}{2}\cos(2\xi)(\sigma_1-\sigma_3) \tag{6}$$

with

$$\xi = \pm\left\{\frac{\pi}{4} + \frac{\phi}{2}\right\}, \tag{7}$$

in which $\phi = \arctan\tilde{\mu}$, and

$$\tilde{\mu} = \frac{ds}{d\sigma} = \left\{\frac{\mu}{\cosh^2\left(\frac{\mu\sigma}{s^*}\right)}\right\}$$

in the above equations, σ_1, and σ_3, are the maximum and minimum principal stresses.

The cohesive strength depends only on the relative density η and is given by the following functional relation,

$$c = \begin{cases} A\eta^m\dfrac{(\eta-\eta_m)}{(1-\eta_m} & \text{if } \eta>\eta_m \\ 0 & \text{if } \eta\leq\eta_m \end{cases} \tag{8}$$

A and m are material constants and η_m, is a characteristic density.

The friction coefficient μ depends on η and the plastic deformation. Its evolution equation is given by,

$$\dot{\mu} = h(\mu)\dot{\gamma}^{(1)}, \text{with the initial condition } \mu(0) = \mu_0 \tag{9}$$

$$h(\mu) = h_\mu\left|\left(1-\frac{\mu}{\mu_s}\right)\right|^p sign\left(1-\frac{\mu}{\mu_s}\right) \tag{10}$$

$$\mu_s = \begin{cases} \mu_{cv} + b(\eta-\eta_{cr})^q & \text{if } \eta>\eta_{cr} \\ \mu_{cv} & \text{if } \eta\leq\eta_{cr} \end{cases} \tag{11}$$

where μ_s is a saturation value of μ.

The quantities p,q,b,η_{cr},μ_{cv} and h_μ are material parameters and the plastic shear strain rate $\dot{\gamma}^{(1)}$ is determined by the flow rule,

$$D^{p^{(1)}} = \dot{\gamma}^{(1)}M^{(1)} \tag{12}$$

$$M^{(1)} = \frac{P + \beta N}{\|P + \beta N\|} \tag{13}$$

$$\beta = h_\beta(\mu-\mu_{cv}) \tag{14}$$

in which h_β is another material parameter. The two tensors P and N are given in terms of $m^{(\alpha)}$ and $n^{(\alpha)}$, viz.,

$$P = sym(m^{(\alpha)}\otimes n^{(\alpha)});\ N = n^{(\alpha)}\otimes n^{(\alpha)} \tag{15}$$

Since $m^{(\alpha)}$ and $n^{(\alpha)}$ are a function of the principal stresses, three cases need to be considered:

case (i) $\sigma_1>\sigma_2>\sigma_3$

$$P = (1/2)\sin(2\xi)\{\hat{e}_1\otimes\hat{e}_1-\hat{e}_3\otimes\hat{e}_3\}, \tag{16}$$

$$N = \{\sin^2\xi\hat{e}_1\otimes\hat{e}_1 + \cos^2\xi\hat{e}_3\otimes\hat{e}_3\}, \tag{17}$$

case (ii) $\sigma_1>\sigma_2=\sigma_3$

$$P = (1/2)\sin(2\xi)\{\hat{e}_1\otimes\hat{e}_1-(1/2)(1-\hat{e}_1\otimes\hat{e}_1)\}, \tag{18}$$

$$N = (1/2)\{\sin^2\xi\hat{e}_1\otimes\hat{e}_1 + (1/2)\cos^2\xi(1-\hat{e}_1\otimes\hat{e}_1)\}, \tag{19}$$

case (iii) $\sigma_1=\sigma_2>\sigma_3$

$$P = (1/2)\sin(2\xi)\{(1/2)(1-\hat{e}_3\otimes\hat{e}_3)-\hat{e}_3\otimes\hat{e}_3\}, \tag{20}$$

$$N = (1/2)\{(1/2)\sin^2\xi(1-\hat{e}_3\otimes\hat{e}_3 + \cos^2\xi\hat{e}_3\otimes\hat{e}_3\}, \tag{21}$$

The second mechanism, called *consolidation* represents the hardening of the media when voids collapse. It has a quarter-elliptical yield surface in the plane $(\bar{p},\bar{\tau})$, where $\bar{p}$ and $\bar{\tau}$ are the mean pressure and the equivalent shear stress, see Fig. 1. The yield condition in this case is:

$$\phi^{(2)} = \sqrt{\left(\bar{p}-\frac{p_c}{2}\right)^2 + \left(\frac{\bar{\tau}}{M}\right)^2} - \frac{p_c}{2} \leq 0 \text{ for } \bar{p} > \frac{p_c}{2} \tag{22}$$

in which p_c is a limiting pressure that depends on the relative density η and M, which is a shape parameter that depends on the material response. In this formulation, p_c is assumed as

$$p_c = \begin{cases} B\eta^n \dfrac{(\eta-\eta_m)}{1-\eta} & \text{if } \eta > \eta_m \\ 0 & \text{if } \eta \leq \eta_m \end{cases} \tag{23}$$

The equation for the pressure cap was modified from the original function given by Gu *et al.* [16] to take into account that for a fully dense material the consolidating pressure becomes unbounded. Note that $p_c \rightarrow \infty$ when $\eta \rightarrow 1$ taking into account that pore collapse cannot occur on a fully densified powder.

The flow rule for the consolidation mechanism is an associated flow rule, namely,

$$D^{p(2)} = \dot{\gamma}^{(2)} M^{(2)}\,;\ M^{(2)} = \partial\phi^{(2)}/\partial T, \tag{24}$$

see Gu *et al.* [16] for additional details.

In addition, the relative density η is calculated from balance of mass, viz.,

$$\dot{\eta} = -\eta \operatorname{trace}(D^{p(1)} + D^{p(2)});\ \eta(0) = \eta_0 \tag{25}$$

The granular model developed by Anand and coworkers [15] has been primarily defined for compressive stress states. Here it is extended to tensile stress states by considering that the mean tensile stress in the material is limited by a value $-p_0$ for which the shear stress is null.

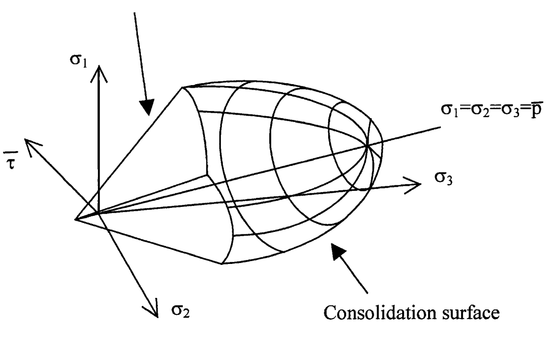

Fig. 1. Yield surface for the granular model.

$$p_0 = -\frac{s^*}{\mu} \tanh^{-1}\left(\frac{c}{s^*}\right) \tag{26}$$

An extended Duvaut-Lions viscoplasticity model (Simo *et al.* [17]) is used to introduce rate dependence in the above plasticity model. In this case the viscoplastic strain rate and internal variables are given by

$$D^{vp} = C^{-1}\left\{\frac{T-\bar{T}}{T_R}\right\};\ q = -\left\{\frac{q-\bar{q}}{T_R}\right\} \tag{27}$$

$$\text{where } (\bar{T},\bar{q}) = \begin{cases} (T,q) & \text{if } \phi^{(1-2)} < 0 \\ \hat{P}(T,q) & \text{otherwise} \end{cases}$$

In these equations, q designates the internal variables vector, $\hat{P}$ is the *closest point projection operator* and T_R is a viscosity coefficient that plays the role of a relaxation time. The visco-plastic deformation rate tensor is proportional to the distance between the stress state T and its projection onto the yield surface. Integration of the above equation leads to the following discrete expressions for the viscoplastic stress and internal variables, viz.,

$$T_{n+1} = \exp(-\Delta t/T_R)T_n + [1-\exp(-\Delta t/T_R)] (\bar{T}_{n+1} + T_{\mathrm{trial}}T_R/\Delta t) \tag{28}$$

$$q_{n+1} = \exp(-\Delta t/T_R)q_n + [1 - \exp(-\Delta t/T_R)]\bar{q}_{n+1} \tag{29}$$

where Δt is the time increment, T_{trial} is the trial stress obtained by assuming elastic response in the increment, and $\bar{T}$ and $\bar{q}$ are obtained from the solution of the rate-independent plasticity problem. Note that for $T_R \rightarrow \infty$ the elastic case is obtained while for $T_R \rightarrow 0$ the rate independent plasticity solution is recovered.

3. CASE STUDIES

3.1. Identification of model parameters: pressure-shear plate impact

Plate impact experiments offer unique capabilities for the characterization of advanced materials under dynamic loading conditions, Espinosa and Nemat-Nasser [23]. These experiments allow high stresses, high pressures, high strain rates and finite deformations to be generated under well-characterized conditions. They all rely on the generation of one-dimensional waves in the central region of the specimen in order to allow a clear interpretation of the experimental results and the mathematical modeling of the material behavior. Inclining the flyer, specimen and target plates, with respect to the axis of the projectile, attains compression-shear loading, see Fig. 2. By

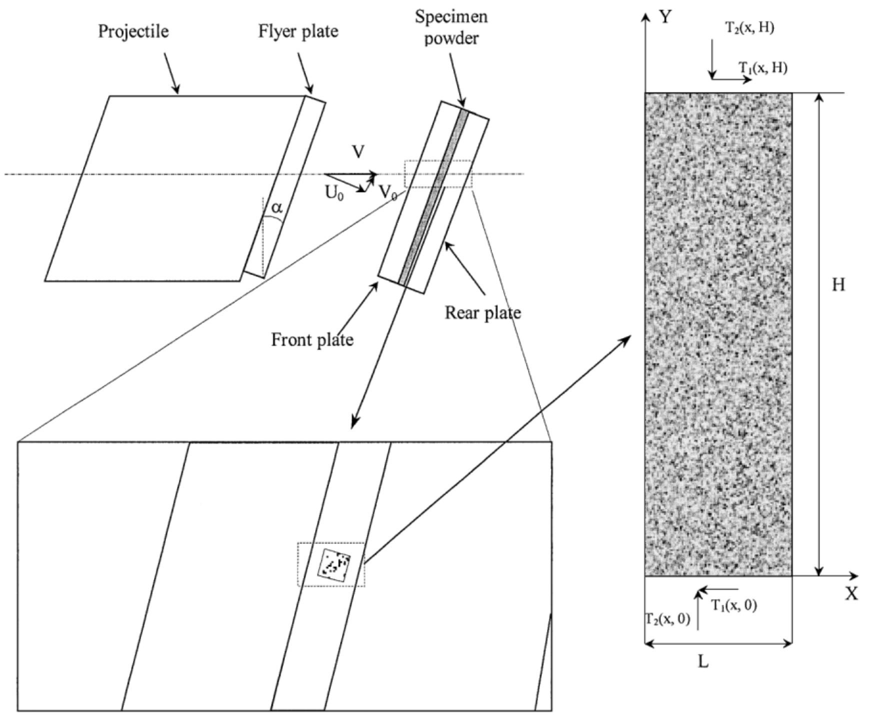

Fig. 2. Pressure-shear plate impact configuration and computational cell.

varying the angle of inclination a variety of loading states may be achieved. In the testing of powder materials, Sairam and Clifton [8] placed the ceramic powder between two anvils. The flyer and the anvils are supposed to remain elastic under the applied loading. The skew angle is selected such that the shear/normal stress ratio is maximized without frictional sliding at the various interfaces. The normal and shear stresses are computed from the measured normal and tangential particle velocities on the back free surface of the rear anvil plate.

At impact, plane compression and shear waves are produced in both the impactor and the target. Because of the difference in wave speeds, the compressive wave arrives first at the powder layer and begins to densify the powder layer before the shear wave arrives. The thickness of the front anvil plate determines the compaction time prior to the arrival of the shear wave to the powder layer. The material studied by Sairam and Clifton was an Alumina (Al_2O_3) powder with purity 99.99%. The average particle size was 0.4 μm.

3.1.1. Boundary and initial conditions. Figure 2 shows the pressure-shear configuration reported by Sairam and Clifton [8]. The specimen is a thin layer 120 μm thick, sandwiched between two anvil plates. The initial relative density of the powder is η=0.378, which corresponds to a density of approximately 1500 kg/m^3. In this configuration the flyer hits the target with an initial velocity V_0 specified in Table 1. The impactor plate is bonded to the front end of a fiberglass tube with the impact planed skewed at the desirable angle.

In order to reduce the computational effort, only a representative volume element is selected as shown on Fig. 2, Zavattieri *et al.* [24]. The front anvil-powder interface is located at $y = H$, while the powder-rear anvil interface is at $y = 0$. Assuming that the computational cell is repeated in the x-direction, the following periodic boundary conditions apply:

$$u(0,y,t) = u(L,y,t), v(0,y,t) = v(L,y,t), \quad a(0,y,t) = a(L,y,t) \tag{30}$$

where u, v and a are the displacement, velocity and acceleration vector fields. Furthermore, assuming that the flyer and the anvil plates remain elastic through out the deformation process, viscous boundary conditions (Espinosa *et al.*, [25]; Zavattieri *et al.*, [24]; Zhou *et al.* [26]) are applied at the top and bottom surfaces of the cell. Conservation of momentum and continuity of velocities and tractions lead to the following equations for tractions t_1 and t_2 at $y = 0$ and $y = H$.

$$t_1(x,H,t) = -(\rho c_s)_{fa}\left[v_1(x,H,t) - \frac{(\rho c_s)_{fa} + (\rho c_s)_c}{(\rho c_s)_{fa}} v_1^0\right] \tag{31}$$

Table 1. Summary of experiments from [8]

Shot no.	Initial impact velocity	Front plate	Rear plate	Flyer plate	Skew angle°
SS-9304	121 m/s	Hampden steel	Hampden steel	Hampden steel	22
SS-9402	145 m/s	Hampden steel	Hampden steel	Hampden steel	22

Table 2. Mass density and impedances of impactor and anvil plates in the pressure-shear impact simulations

Material	Longitudinal wave speed (m/s)	Transverse wave speed (m/s)	Acoustic impedance $\left(\frac{\text{Gpa}}{\text{mm}/\mu\text{s}}\right)$	Shear impedance $\left(\frac{\text{Gpa}}{\text{mm}/\mu\text{s}}\right)$	Mass density (kg/m^3)
Hampden tool steel	5983	3264	45.50	24.90	7612

$$t_2(x,H,t) = -(\rho c_l)_{fa}\left[v_2(x,H,t) - \frac{(\rho c_l)_{fa} + (\rho c_l)_c}{(\rho c_l)_{fa}}v_2^0\right]$$

$$t_1(x,0,t) = -(\rho c_s)_{ra}v_1(x,0,t)$$

$$t_2(x,0,t) = -(\rho c_l)_{ra}v_2(x,0,t)$$

where $()_{fa}$, $()_{ra}$, and $()_c$ denote front anvil, rear anvil and ceramic quantities, c_l and c_s are the longitudinal and shear wave speeds, ρ is the specific material density, v_1 and v_2 are in-plane and normal velocities and $v_1{}^0$ and $v_2{}^0$ are the in-plane and normal velocities at the front anvil-powder interface upon arrival of the shear and normal waves, respectively.

The initial in-plane and normal velocities at the rear anvil-powder interface are zero and at the front anvil-powder interface are given by,

$$v_1^0 = \frac{(\rho c_s)_{fa}}{(\rho c_s)_{fa} + (\rho c_s)_c}\cdot\frac{2(\rho c_s)_f}{(\rho c_s)_f + (\rho c_s)_{fa}}V_0\sin\gamma \tag{32}$$

$$v_2^0 = \frac{(\rho c_l)_{fa}}{(\rho c_l)_{fa} + (\rho c_l)_c}\cdot\frac{2(\rho c_l)_f}{(\rho c_l)_f + (\rho c_l)_{fa}}V_0\cos\gamma$$

in which $()_f$ denotes flyer quantities.

The material properties of the steel flyer and anvil plates are given in Table 2.

3.1.2. Results and discussion. According to [8], the thickness of the front anvil plate was chosen such that the powder specimen is fully compacted before the shear wave arrives to the specimen. In this way, it is possible to study separately the compaction mechanism and the shearing mechanism.

Figure 3 shows the normal stress history as reported in [8]. The slow build up in pressure, as recorded by a normal velocity interferometer, results from compaction of the powder layer. At early stages, the particles make contact at isolated points, which is very inefficient for wave propagation. Upon wave reverberations in the specimen, voids are collapsed and the number of contact points, between particles, increases monotonically. The normal stress build up, interferometrically recorded, provides a measure of the pressure cap in the consolidation mechanism as a function of powder density. When the powder is fully compacted, the record provides insight into the mechanical behavior of the densified powder material.

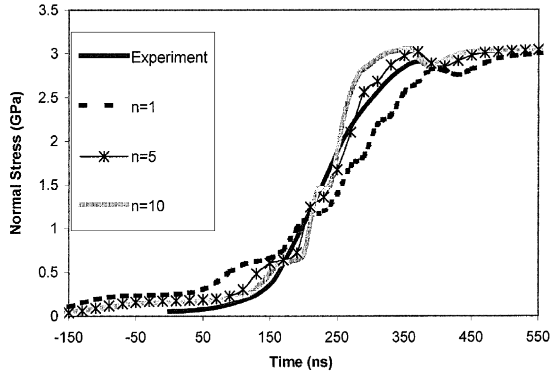

Fig. 3. Experimental normal stress history from shot SS9402 and numerical simulations for different values of *n*. Simulations are performed with T_R=0.1 picoseconds.

During compaction, the simulations show no significant *macroscopic* shearing in the specimen. According to equation (22) the equivalent shear stress is null. Only the expression of p_c , shown in equation (23) plays a significant role. Furthermore, the value of η_m, can be determined in a straight forward manner; it is the value of the relative density for which the normal stress begins to increase. The value of the relative density can be inferred from the measurement of sound speed in the powder. Unfortunately, Sairam and Clifton [8] did not report such a measurement. Nevertheless, the stress profile they reported for shot SS-9402, shows a non null normal stress at time t=0 and a slow rising normal stress after that (see Fig. 3). We assume that η_m is slightly lower than the initial relative density. A value of $\eta_m = 0.3$ has been used in the calculations.

The value of coefficient B in equation (23) determines the level of the pressure cap for small relative densities. Unfortunately, this portion of the curve is missing in the results reported by Sairam and Clifton [8]. It has been decided to keep B=500 MPa as proposed by Anand and Gu [15] for MH-100 iron powder.

The slope of the normal stress, in the rising part, is then essentially determined by the value of n since p_c depends on η^n see Fig. 3. The best fit is obtained for $n = 5$. The steps seen in the numerical simulations are not observed in the experimental records. These steps correlate with the time the longitudinal wave takes during a round trip in the powder layer. In the case of $n = 5$, the steps are less pronounced but still present. Since Sairam and Clifton [8] did not report the delay time used in the normal velocity interferometer, it is not possible to determine if the signal represents and average over a period of time longer than the duration of the steps in our calculations. It should be noted that the amount of data reported in the literature, on the dynamic compaction and shearing of ceramic powders, is very limited.

Parameter M, see (equation (22)), defines the shape of the pressure cap. If too big, the distortion mechanism is inhibited and the simulation cannot retrieve the correct yield shear stress. Here we adopt a value of $M = 0.6$.

The shear strength measured by Sairam and Clifton [8], using a transverse displacement interferometer, in shot SS-9304, is about 510 MPa. Considering that the pressure is about 2.5 GPa, we assume that the shear strength saturation value $s^* + c$ given by equation (4) is reached. Since we believe that cohesion in a ceramic powder is low, the value of s^* is assumed to be 500 MPa and c=10 MPa.

The coefficients introduced in equations (9–11) can be experimentally determined if the thickness of the front plate is thin enough so that shearing occurs during powder compaction. The curve $\mu = f(\eta)$ can be approximated by these equations. This was not the case in the results reported by Sairam and Clifton [8]. The coefficients h_μ, p, q, b and μ_{cv} are kept the same as those proposed by Anand and Gu [15] for dry sand.

Finally it has been noticed that the shear yield strength is highly sensitive to the relaxation time T_R, see Fig. 4. From the various simulations reported in (Fig. 4), for a relaxation time of about 0.1 picoseconds the best fit is obtained. Therefore, the powder constitutive behavior appears to be quite rate independent, which is consistent with the deformation mechanisms. When the relaxation time is 1 picosecond, the shear stress history in the first 200 nanoseconds exhibits variations similar to the measured shear stress history. Therefore, a lower value of s^* and a higher relaxation time may produce a better fit concerning the shear stress history. However, it was observed that the normal velocity history is over predicted when such set of parameters is used. More experimental results at various strain rates are required for a more precise identification of model parameters.

3.2. Simulations of cylinder collapse experiments

In this investigation we use the cylinder collapse technique to examine the validity of the granular model and its capabilities to capture dynamic shear localization.

The thick-walled-cylinder collapse experiment has been developed initially for research on solids, Nesterenko *et al.* [27, 28] and porous materials, Nesterenko *et al.* [29, 30]. Later, Nesterenko *et al.* [11] used the thick-walled cylinder collapse experiment to examine the formation of shear localization in granular media under high strain rate, high pressure and large strain conditions.

These investigators found that granular Alumina subjected to strains between 0.2 and 0.4 at a strain rate of $3\times10^4\ s^{-1}$ exhibited profuse shear-band formation. They extended their study to fragmented and granular Silicon Carbide in Shih *et al.* [12, 13]. They also found that spacing, displacement and formation of shear bands are determined by the particle size.

The experimental configuration is shown in Fig. 5. A hollow cylinder of ceramic is placed in a tubular cavity between a central copper rod and an outer copper tube. An explosive with a low detonation velocity is used to densify or fracture the ceramic. Detonation is initiated at the top of the charge and propagates along the cylinder axis. A cylindrical hole is drilled along the longitudinal axis of the copper rod and this composite cylinder is collapsed by detonation of a second cylindrical explosive charge with a high detonation velocity. This second explosive event produces significant plastic deformation in the densified material. The deformation is highly localized within shear bands, see Fig. 5.

The previously determined model coefficients are used to simulate the thick-walled-cylinder collapse experiments reported in Nesterenko *et al.* [27]. Two materials are considered, Al_2O_3 and SiC powders. For the SiC powder, all the model coefficients reported in Table 3 remain the same as Al_2O_3, except for the initial density and the elastic properties.

3.2.1. Boundary and initial conditions. In this section we describe the computational model used in the simulations. Only the second explosive event is simulated. The initial radii of the tubes, which define the computational cell, are given in Table 4. The corresponding relative density is 85% for the SiC powder and 84% for the Al_2O_3 powder.

The load history resulting from the explosive charge is not measured experimentally. Hence, in the simulations an applied pressure on the external wall of the outer tube is used to simulate the explosive load. The load history is plotted in Fig. 6. It has two ramps with durations of 4 μs each. The copper tubes are modeled with a Zerilli-Armstrong law [31] and the pressure is computed with a Mie-Gruneisen equation of state. The material parameters used to model Copper are given in Table 5. The granular material

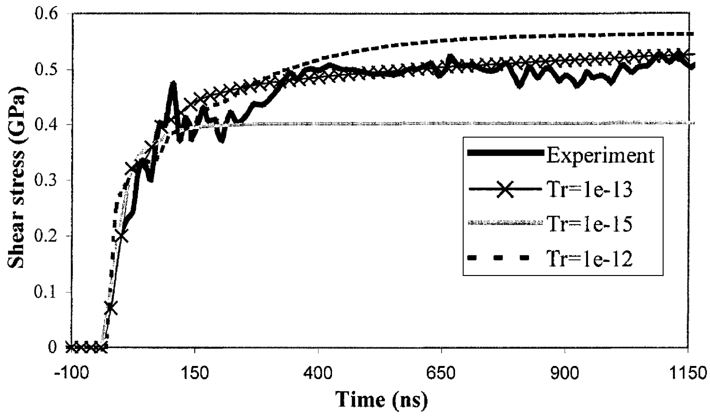

Fig. 4. Shear strength history from shot SS-9303 and simulation for different values of T_R in seconds.

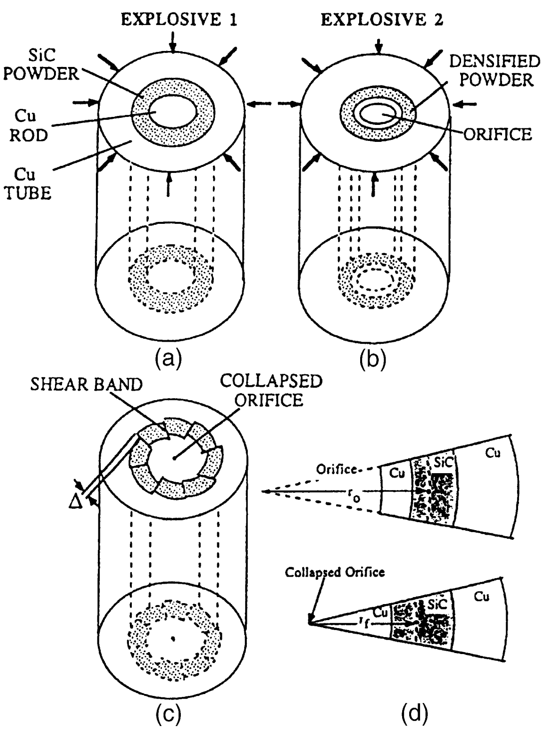

Fig. 5. Experimental steps for densification and deformation of granular ceramic, (a) Explosive event 1: densification; (b) explosive event 2: deformation; (c) final configuration; (d) initial and final radii during deformation, Nesterenko *et al.* [27].

properties and model parameters were given in Table 3.

In order to reduce the computational effort, only a slice of the rings is model and periodic boundary conditions applied. A typical sector defined by an angle of 15° is chosen. It has been verified that when an angle of 30° is utilized the same results are obtained. Assuming that the computational cell is repeated in the θ-direction, the following periodic boundary conditions are applied:

$$u(r,0°,t) = u(r,15°,t)$$
$$v(r,0°,t) = v(r,15°,t) \quad (33)$$
$$a(r,0°,t) = a(r,15°,t)$$

Because of the periodic boundary conditions, it has not been possible to use remeshing, in the inner copper ring, in LS-DYNA. Consequently, a total collapse of this ring is not possible and a cylindrical rigid wall is applied at a radius r_w=0.5 mm to prevent elements to collapse.

The effect of cell size is investigated using three typical element sizes. For the SiC powder, elements 100 μm, 50 μm and 25 μm in size are employed. For the Al_2O_3 powder, a mesh with a 50 μm element size is used.

3.2.2. Results and discussion. Figure 7 shows contours of plastic strain resulting from the distorsion mechanism for three meshes with decreasing element size. The simulations capture the array of shear-bands experimentally observed by Nesterenko *et al.* [23] independently of the element size, see Fig. 7. On this figure the bands are revealed by high gradients in accumulated plastic shear strains due to the distortion mechanism. The resolution of the bands is improved with mesh refinement. Furthermore, the angle between two sets of bands increases from the inner radius to the outer radius. These angles are in agreement with the angles measured by Nesterenko *et al.* [23], in the case of fine SiC powder, see Fig. 8. The simulations also capture the double pattern of clockwise and counter clockwise shear bands. However, the shear strain and the thickness of the bands remain highly dependent of the element size despite the fact that the model is rate dependent. Thickness and spacing for each mesh are reported in Tables 6 and 7. The spacing is corrected to take into account that only a slice with an opening angle of 15° is simulated. It is measured between the centers of two adjacent bands within the computational cell. The thickness is measured as the distance between two points for which the plastic shear strain due to the distortion mechanism, $\gamma^{(1)}$, is 95% of the maximum plastic shear strain for this band. However, only one Gauss point is used :in each element. Consequently, the thickness of the band

Table 3. Material coefficients determined for Al_2O_3 powder with an average grain size of 0.4 μm

Material's properties	Symbol	Units	Al_2O_3
Initial Young's modulus	E	GPa	374
Initial Poisson's ratio	ν	–	0.22
Initial density	ρ	Kg/m^3	3970
Shape parameter for Young's modulus	E_2	–	3.6619
Shape parameter for Poisson's ratio	ν_2	–	0.18149
Consolidation mechanism	B	MPa	500.0
	n	–	5.0
	η_m	–	0.3
	M	–	0.6
Distortion mechanism	m	–	3.0
	h_μ	–	300.0
	p	–	1.88
	μ_{cv}	–	0.05
	b	–	0.071
	q	–	1.0
	η_{cr}	–	0.3
	h_β	–	2.5
Relaxation time	T_R	s	10^{-13}

Table 4. Initial configurations for cylinder collapse experiments

	SiC powder (mm)	Al_2O_3 powder (mm)
Inner radius of inner copper tube	5.5	5.5
Outer radius of inner copper tube	8	8
Inner radius of external copper tube	11	9
Outer radius of external copper tube	12	10

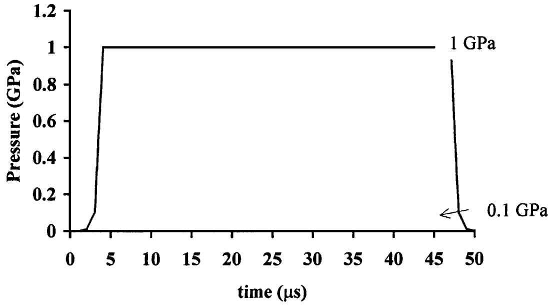

Fig. 6. Profile of pressure load applied on external face of outer copper ring.

is known with a possible variation of two elements length, i.e. 200 μm, 100 μm or 50 μm, respectively.

The shear instability begins at the interface between the inner copper cylinder and the ceramic powder. Similar results were already reported by Nesterenko *et al.* [23] on shear-band initiation in titanium. According to Nesterenko *et al.* [11] initiation occurs sooner with small particle size than with coarse particle size. The coefficients in our simulations have been determined for a 0.4 μm Alumina powder. An early stage initiation is expected. In fact initiation occurs in all cases after only 2 μs, i.e., as soon as the pressure wave reaches the ceramic layer. The shear strain in the band continues to increase until the pressure in the specimen is homogenized 40 to 50 μs later, see Fig. 9.

The simulated bands propagate with a mean velocity of about 2000 m/s in the SiC powder and 1600 m/s in the Al_2O_3 powder, but the intensity of the shearing decreases as the radius increases. Moreover, each crossing between two perpendicular sets of bands contributes to decrease the shear strain. According to Nesterenko *et al.* [23], this phenomenon is indicative of cooperative material motion and self organization among the bands that leads to the formation of two to four groups of the clockwise and counterclockwise shear bands. Because only 15° of the geometry is represented, crossing between perpendicular bands occurs more often than in reality in the SiC geometry. This could be a reason for the almost disappearance of the bands nearby the outer radius of the ceramic cylinder. Nevertheless, it is clearly visible on Fig. 7 that a main band group develops.

The measurement of band thickness in the simulation is quite approximate to be meaningfully compared to the band thickness observed in experiments. However, the band spacing is accurately captured and the simulations are in close agreement with the experimental values.

The partitioning of total strain (e_t) into homogeneous deformation (e_b) and deformation localized in shear bands (e_s) was carried out in a manner identical to the on described by Nesterenko *et al.* [11]. About 18 μs after the loading is applied, the collapse of the inner copper ring is total and the inner radius of the ceramic layer does not evolves significantly. The final homogeneous deformation for the Alumina powder is exactly the same as measured in the experiment. But the final homogeneous deformation of the

Table 5. Material properties and model parameters for copper rings

Material's properties	Symbol	Units	Copper
Density	ρ	Kg/m^3	8600
Young Modulus	E	GPa	125.0
Poisson's ratio	v	–	0.359
Zerilli-Armstrong model [31]			
$\sigma = C_1 + \{C_2(\varepsilon^p)^{1/2}[e^{-C_3 + C_4 \ln(\dot{\varepsilon}^*))T}] + C_5\}$			
$\dot{\varepsilon}^* = \dot{\varepsilon}/\dot{\varepsilon}_0; \dot{\varepsilon}_0 = 1s^{-1}$			
Model Constants	C_1	MPa	46.5
	C_2	MPa	890
	C_3	–	0.0028
	C_4	–	1.15 10^{-4}
	C_5	MPa	0
$P = \dfrac{\rho_0 C^2\mu\left[1 + \left(1-\frac{\gamma_0}{2}\right)\mu - \frac{a}{2}\mu^2\right]}{\left[1-(S_1-1)\mu - S_2\frac{\mu^2}{\mu+1} - S_3\frac{\mu^3}{(\mu+1)^2}\right]} + (\gamma_0 + a\mu)E_n$ for compressed materials			
$P = \rho_0 C^2\mu + (\gamma_0 + a\mu)E_n$ for expanded materials			
$\mu = \rho/\rho_0 - 1$			
EOS Parameters	C	m/s	3958
	S_1	–	1.497
	S_2	–	0
	S_3	–	0
	γ_0	–	2.0
	a	–	0
	E_{n0}	J/kg	0
Linear Artificial Viscosity	C_L	–	1.5
Quadratic Artificial Viscosity	C_Q	–	0.06
Specific Heat	C_p	J/Kg/K	400

SiC ceramic layer is e_t=−15% independently of the mesh size. The experimental result was e_t=−21%. The difference can be explained because the loading applied in the simulation is idealized and does not accurately reflect the real explosive loading. In particular, the applied pressure in the experiment was certainly higher than 1 GPa. It is also possible that the collapse of the inner copper ring is not well reproduced because of the existence of the rigid wall. The steps in plastic deformation observed in Fig. 9, reveal release waves originating from the artificial free surface. However, the localized deformation in the form of shear bands, for the medium size mesh simulations, is close to the experimental values. As previously mentioned, more pressure-shear experimental data, at various strain rates, is needed to properly identify the relaxation time used in the viscoplasticity model. This parameter plays a critical role in obtaining a mesh independent solution.

4. CONCLUDING REMARKS

The model for granular materials proposed by Anand and co-workers [15] has been modified to include time dependence, through a relaxation parameter, and incompressibility at zero void ratios. The parameters of the model, for granular Al_2O_3 with a fine grain size (0.4 μm), are determined by means of simulating pressure-shear plate impact experiments. These parameters are used afterward to simulate the thick-wall-cylinder collapse experiment developed by Nesterenko *et al.* [11, 23]. The model parameters are kept the same to simulate the behavior of granular Silicon Carbide, except for the elastic properties. The numerical simulations capture the shear-banding pattern observed in the experiments. Initiation and propagation of bands are similar to the experimentally observed phenomena. Significant information is gained from these simulations such as the initiation site of shear bands and their propagation speed. Furthermore, the evolution of field variables is obtained from the simulations.

The model success in capturing shear localization is based on the competition between powder compaction and dilatancy. The former resulting from particle re-arrangement with increasing pressure and the latter from shearing of powder particles. Equally important is the friction coefficient evolution as a function of powder density and distortional plastic strain rate.

One the major observations from the present simulations was the variation in band separation and width

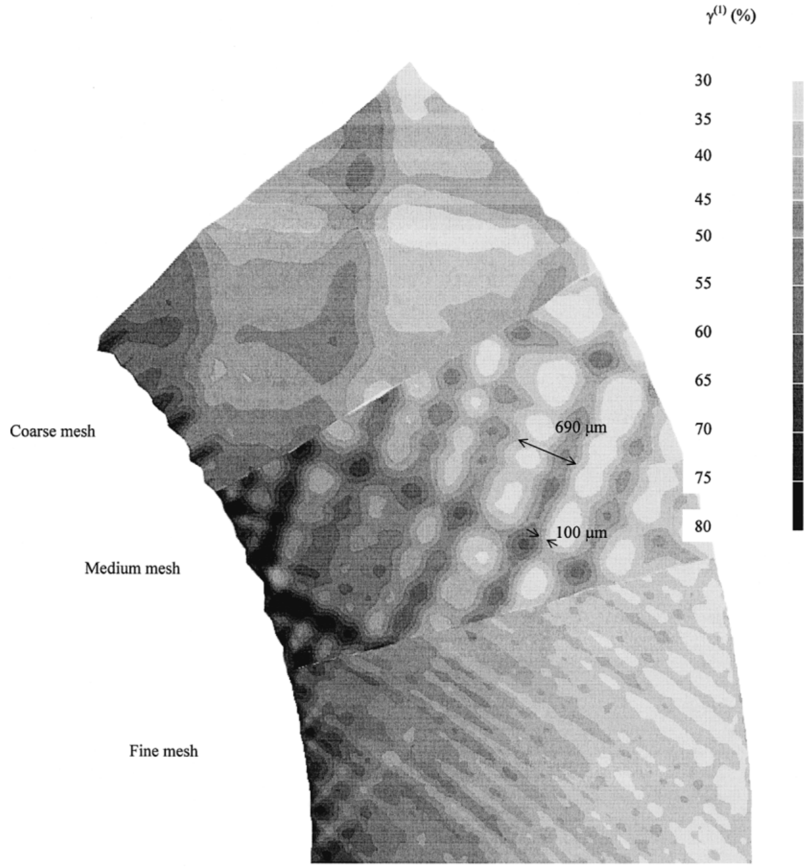

Fig. 7. Simulation of cylinder collapse experiment for fine 0.4 μm average particle size SiC powder. Contours of plastic strain due to the distortion mechanism, $\gamma^{(I)}$. Shear bands are thinner and more numerous as the mesh size decreases. A relaxation time of 0.1 picosecond is used in the simulations.

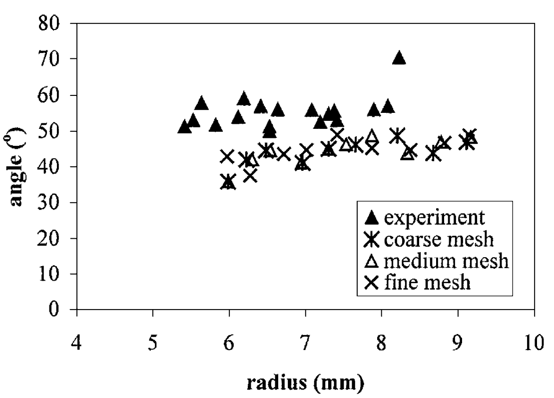

Fig. 8. Plot of tangential angle as a function of radial distance for the 0.4 μm grain size SiC powder. Experimental results are included for comparison purposes, from Nesterenko *et al.* [23].

with mesh size. The solution seems to converge slowly as the element size approaches the particle size. Finer meshes are not justified from a continuum standpoint. Despite the fact that the constitutive equations were regularized using the Duvaut Lions scheme, the identified relaxation time, by means of simulations of the pressure-shear experiments, is too small resulting in an almost rate independent behavior. It is know that rate independence results in mesh dependence in localization problems. Hence, the formulation of non-local constitutive laws of the type postulated by Aifantis and co-workers or Hutchinson and co-workers may need to be investigated in this regard. A cautionary remark is here appropriate. The experimental information reported in the literature is very limited and incomplete. Very few pressure-shear experiments on powder ceramics have been conducted and there is no single experimental result in which both axial and shear stress histories are reported for the same experiment. Moreover, the real-time data obtained in cylinder collapse experiments is very limited and the explosive pressure waves are a phenomenon difficult to model with high accuracy. Before additional high quality experimental measurements are obtained, the development of more complex constitutive laws may result in futile efforts. As mentioned in the discussion of the simulations, the available data is not enough to uniquely determine a set of parameters and in particular the material relaxation time. Despite these limitations, the examined model captures the main physical features observed experimentally.

The model here discussed was used in conjunction with a microcracking multi-plane model to simulate

Table 6. Comparison of band spacing, thickness, strains and band propagating velocity for the SiC ceramic powder

	Simulations			Experiments		
	Coarse mesh	Medium mesh	Fine mesh	particle size=50 μm	particle size=3 μm	particle size=0.4 μm
Band thickness (μm)	≈500	≈100	≈100	40	25	15
Band spacing (mm)	1.500	0.690	0.500	0.619	1.033	0.525
Average number of bands	24	96	144	51	29	58
Total displacement (μm)	803	1624	–	0	2820	1950
Global tangential strain	−15%	−15%	−15%	−20.5%	−21.4%	−21.6%
Shear-band strain	−12%	−2.4%	–	0	−3.8	−2.6
Band velocity (m/s)	≈1000	1900	2065	–	–	–

Table 7. Comparison of band spacing, thickness, strains and band propagating velocity for the Al_2O_3 ceramic powder

	Simulations	Experiments	
	Medium mesh	particle size=4 μm	particle size=0.4 μm
Band thickness (μm)	400	11	11
Band spacing (mm)	0.96	0.61	0.49
Total displacement (μm)	3285	–	–
Global tangential strain	−22%	−22%	−22%
Shear-band strain	−5.7%	−4%	−8%
Band velocity (m/s)	1600	–	–

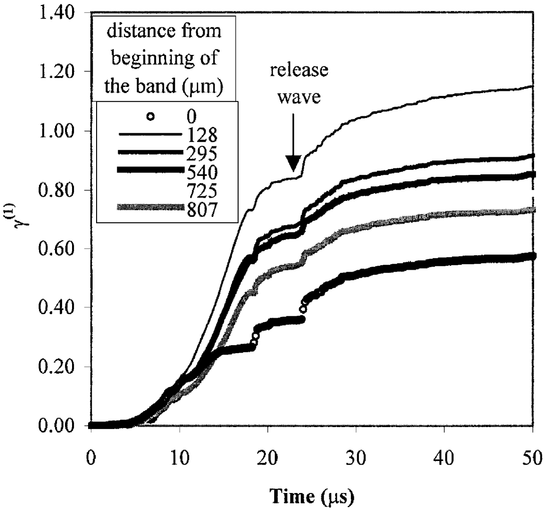

Fig. 9. Evolution of plastic strain, resulting from distortion mechanism, at different points along a shear band. The shear band initiation point is used as origin of the arc length coordinate.

ballistic penetration of ceramic tiles. The model is able to capture the transition between interface defeat and full penetration as a function of long rod tungsten heavy alloy impact velocity. Material evolution from a pristine state to a fully pulverized ceramic is mathematically described with the algorithms here presented, see Gailly and Espinosa [14] for details.

Whereas the present discussion is confined to ceramic material, the granular model has been applied to various materials including sand, copper and steel powders, see Gu *et al.* [16] and Anand and Gu [15]. The model should be equally applicable to various soil and concrete materials.

Acknowledgements—This research was supported by the Army Research Office through ARO-MURI Award No. DAAH04-96-1-0331 and by the Delegation Generale pour l'Armement through decision No. 21132/DGA/DSP/D. The authors would like to add a special thanks to Prof. Anand for providing the latest developments on his granular model.

REFERENCES

1. Mescall, J. and Weiss, V., Materials Behavior under High Stress and Ultrahigh Loading Rates-Part II, in *Proceeding 29th Sagamore Army Conference*. Army Materials and Mechanics Research Center, Watertown, MA, USA, 1984.
2. Shockey, D. A., Marchard, A. H., Skaggs, S. R. *et al.*, *Int. J. Impact Engng.*, 1990, **9**(3), 263.
3. Hauver, G., Netherwood, P., Benck, R. and Kecskes, L., Ballistic Performance of Ceramic Targets, in *Proceedings of Army Symposium on Solid Mechanics*. Plymouth, MA, USA, 1993.
4. Hauver, G., Netherwood, P., Benck, R. and Kecskes, L., Enhanced Ballistic Performance of Ceramics, in *Proceedings of 19th Army Science Conference*. Orlando, FL, USA, 1994.
5. Rapacki, E., Hauver, G., Netherwood, P, and Benck, R., Ceramic for Armors - A Material System Perspective, in *Proceeding of 7th Annual TARDEC Ground Vehicle Survivability Symposium*. 1996.

6. Klopp, R. W. and Shockey, D. A., *J. Appl. Phys.*, 1991, **70**(12), 7318.
7. Espinosa, H. D. and Clifton, R. J., in *Symposium on Experiments in Micromechanics of Fracture-Resistance Materials*, ed. K. S. Kim. ASME Winter Annual Meeting, Atlanta, GA, USA, 1991, p. 37.
8. Sairam, S. and Clifton, R. J., ASME AMD-Vol. 197, in *Mechanical Testing of Ceramics and Ceramic Composites*, ed. A. Gilat. 1994, p. 23.
9. Sairam, S. and Clifton, R. J., ASME AMD-Vol. 219, in *Advances in Failure Mechanisms in Brittle Materials*, ed. R. J. Clifton and H. D. Espinosa. 1996, p. 59.
10. Sairam, S. and Clifton, R. J., *Mech. mater.*, 1997, **29**, 233.
11. Nesterenko, V. F., Meyers, M. A. and Chen, H. C., *Acta mater.*, 1996, **44**(5), 2017.
12. Shih, C. J., Meyers, M. A. and Nesterenko, V. F., *Acta mater.*, 1998, **46**(11), 4037.
13. Shih, C. J., Nesterenko, V. F. and Meyers, M. A., *J Appl. Phys.*, 1998, **83**(9), 4660.
14. Gailly B. A. and Espinosa H.D., *Num. Meth Engng.*, 2000, submitted.
15. Anand, L. and Gu, C., *J. Mech. Phys. Solids*, 2000, **48**, 1701.
16. Gu, C., Kim, M. and Anand, L., *Int. J. of Plasticity*, 2001, **17**, 147.
17. Simo, J. C., Kennedy, J. G. and Govindjee, S., *Int. J. Num. Meth. Engng.*, 1988, **26**, 2161.
18. Budianski, B., *Journal of Composites*, 1970, **4**, 286.
19. Spencer, A. J. M., *J. Mech. Phys. Solids*, 1964, **12**, 337.
20. Spencer, A. J. M. in *Mechanics of Solids*, ed A.J.M. Spencer, H. G. Hopkins, and M.J. Swewell. Pergamon Press, Oxford and New York, 1982, p. 607.
21. Mehrabadi, M. M. and Cowin, S. C., *J. Mech. Phys. Solids*, 1978, **26**, 269.
22. Nemat-Nasser, S., Mehrabadi, M. M. and Iwakuma, T., in *Three Dimensional Constitutive Relations and Ductile Fracture*, ed. S. Nemat-Nasser. North-Holland, Amsterdam, 1981, p. 157.
23. Espinosa, H. D., and Nemat-Nasser, S., *ASM Handbook*, Vol. 8, 2000.
24. Zavattieri, P. D., Raghuram, P. V. and Espinosa, H. D., *J. Mech. Phys. Solids*, 2001, **49**(1), 27.
25. Espinosa, H. D., Raiser, G., Clifton, R. J. and Ortiz, M., *J Appl. Phys.*, 1992, **72**, 3451.
26. Zhou, M., Needleman, A. and Clifton, R. J., *J. Mech. Phys. Solids*, 1994, **42**(3), 423.
27. Nesterenko, V. F., Meyers, M. A. and Wright, T. W., *Acta mater.*, 1998, **46**(1), 327.
28. Nesterenko, V. F. and Bondar, M. P., *DYMAT Journal*, 1994, **1**, 245.
29. Nesterenko, V. F., Meyers, M. A., Chen, H. C. and LaSalvia, J. C., *Appl. Phys. Lett*,, 1994, **65**, 3069.
30. Nesterenko, V. F., Meyers, M. A., Chen, H. C. and LaSalvia, J. C., *Metall. Mater. Trans. A*, 1995, **26A**, 2511.
31. Zerilli, F. J. and Armstrong, R. G., *J. Appl. Phys.*, 1987, **61**(5), 1816.